



DOI: 10.19187/abc.202073189-201

Novel Approach Exploiting the Hyperspectral Imaging System for Breast Cancer Therapy and Diagnosis

Mohamed Hisham Aref^{f*}, Ibrahim H. Aboughaleb^a, Abou-Bakr M. Youssef^b,
Yasser H. El-Sharkawy^a

^a Biomedical Engineering Department, Military Technical College, Cairo, Egypt

^b System & Biomedical Engineering Department, Cairo University, Giza, Egypt

ARTICLE INFO

Received:

07 October 2020

Revised:

26 October 2020

Accepted:

29 October 2020

Key words:

Breast cancer,
hyperspectral imaging system,
tissue optical properties,
breast diagnosis & therapy,
optical spectroscopy

ABSTRACT

Background: Breast malignant growth is the most widely recognized disease in women in both highly and less developed nations where early detection is vital for life-saving and fast recovery. Recently, Photonic technologies has played a vital role in medical applications. Their satisfactory and viable implementation in therapy and diagnosis requires reliable information on the optical properties of human tissues. This study presents an outline of recent outcomes on the magnitude of breast tissue optical properties.

Methods: We established two different system setups utilizing hyperspectral (HS) camera and multiple excitation source lights with wavelength (380~1050 nm) for this investigation. The first setup (Transmission Mode) was applied for light transmission measurement of *ex-vivo* breast sample. Thereby, we made calculations of sample absorption. The second setup (Reflection Mode) was used for the measurement of breast sample light diffuse reflectance. The outcomes of both setups were used to select the optimum spectral image to differentiate between the normal and tumoral regions in the *ex-vivo* breast sample by exploring the optical properties spectroscopy in the Near and visible (NIR-VIS) spectrum. Finally, we applied the custom system on the case study technique for breast tumor detection.

Results: Experimental investigations results showed that due to the various excitation wavelength light source (380~1050 nm) generates variable depths of penetration depth in the *ex-vivo* breast sample. Consequently, experimental results of the diffuse reflectance (R_d) provide the optimum spectral image at 600 nm for the diagnostic applications. However, the statistical calculation of the normalized signal validated the outcome at wavelength 680 nm. Additionally, we noticed the optimum spectral image for therapy applications at 700 nm by measurement of breast tissue transmission (T) and attenuation absorption (A) calculation. Moreover, the statistical calculation of the normalized signal validated the outcome at wavelength 760 nm.

Conclusions: The proposed novel approach successfully provided promising results of the investigated breast sample optical properties in both diagnostic and therapy applications to assist the pathologist and the surgeon. The trail outcomes of the investigated case study were impressive for selecting optimum wavelength for diagnostic and treatment (680, 760 nm), respectively.

Introduction

Cancer is the second leading cause of death after heart disease as it continues to threaten the lives of millions worldwide.^{1, 2} In males, the most leading cause of cancer death is lung cancer. However, in females, breast cancer is mostly the leading cause of

Address for correspondence:

Mohamed Hisham Aref, MSc.
Address: Building 3, Block No 7078, El-Mokattam, Cairo, Egypt
Postal Code: 11571
Tel:+2 01221997009
Email: mh-aref@ieee.org



mortality.³ Breast cancer is the most widely recognized malignant disease in women in both highly and less developed nations.^{3,4} More than 8% of women will endure this disease during their lifetime.⁵ Breast cancer is a malignant tumor that is established from cells in the breast some times with no symptoms in early stages.⁶

Breast cancer rate increases with age from the 3rd to the 5th decade.⁷ Of all breast malignant growth, 90 to 95% cases are found through breast self-assessment.⁸ As indicated by the World Health Organization (WHO) in 2018, it is evaluated that 627,000 women died from breast malignant growth, which is roughly 15% of all malignant deaths among women.⁹

Numerous common imaging techniques can be utilized for breast malignant growth analysis such as X-ray Mammograms,^{10,11} Breast Ultrasound^{7,12}, and Breast MRI.^{13,14} However, it is strengthened by several components such as the Contrast to Noise Ratio¹⁵, spatial resolution, and Signal to Noise Ratio of each device.¹⁶

The regular imaging technique for breast screening and examinations in various countries is x-ray mammography.¹⁷ However, its sensitivity is ~74% and is reduced down to ~50% in dense breast, beside manipulating x-ray radiation dosages¹⁸ while Breast MRI provides high sensitivity but its specificity is relatively poor. Additionally, it is characterized by being costly and long examination time.^{19,20}

Currently, biopsy is the best technique for tumor identification, which incorporates the resection of tissue from the breast lesions which is then analyzed by a pathologist.²¹ However, it is expensive, tedious (staining, slicing, and microscopic examination) and requires exceptionally prepared specialists and pathologists.²²

Whole tumor resection is challenging as a result of the absence of perfect intraoperative tumor margin imaging systems.²³ Thus, in up to 37% of female patients encountering breast conserving surgery procedure, the tumor exists in the resection margins of the resected specimen.^{24,25} This increases the risks of tumor recurrence and long recovery endurance.²⁶ Now, a pathologist, who examines the tissue under an advanced microscope, assesses the resection margins a few days after a surgery. In this manner, there are few prompt analysis can give direct information to the specialist in real-time surgery.²⁷

Lately, numerous scientists have set up various methods for resection margins evaluation during breast-conserving surgery (frozen section analysis, ultrasound, imprint cytology, and sample radiography) to decrease the amount of tumor-positive resection margins.²⁸⁻³⁰ On the other hand, none of these techniques have been available and effective for clinical use. The “frozen section analysis” could be done within ~30 mins, with a

sensitivity and specificity of 83% and 95%, respectively.²⁸

The main drawbacks of the technique involves the necessity for a particular pathologist, risk of false negatives (FN), and the impracticability of examining the entire surface of resection margins^{29,30} In the imprint cytology technique diagnose could be established within ~15 mins, with a sensitivity and specificity of 72% and 97%, respectively. The information elucidation errors, sample surface irregularity, and dryness are the drawbacks of this technique.²⁸

Hyperspectral imaging (HSI) is also called imaging spectroscopy, which reveals the novelty that integrates typical imaging and spectroscopy modalities to secure both spatial and spectral data of an item.^{31,32} Imaging spectroscopy has been accessible as a far off detecting innovation since the 1960s.³³ Several studies discussed the HSI capabilities in distinguishing red meats quality³⁴, and its relevance in excellence and safety inspections of the grains and nuts.³⁵ Moreover, utilizing HSI in the near-infra red (NIR) wavelengths in agriculture and food crops has produced superior results.³⁶

Furthermore, for the medical applications exploiting HSI, subsequent studies revealed the efficiency of HSI in non-invasive tissue examinations³⁷, in the tumor detection in *ex-vivo* samples of head and neck for human being tissues³⁸, the usage of HSI with non-contact endoscopic system to detect colorectal cancer³⁹, detection of skin cancer⁴⁰, and breast tissue.^{27,40}

A study was conducted to highlight the unique properties of HSI in radiofrequency ablation (RFA).⁴¹ Aref et al. showed that HSI could be a powerful tool in distinguishing thermal ablation of 10 samples of the *ex-vivo* bovine liver due to the variations of the optical properties, with the trials showing an ideal spectral image (720 ± 18.92 nm).⁴¹

Moreover, the HSI system was exploited to determine malignant growth in the *ex-vivo* breast samples. The outcomes of the segmented spectral regions (420~620 nm) were efficient to distinguish the cancerous region from the normal tissue with 95%, and 96% sensitivity, and specificity, respectively.⁴² Additionally, the HSI system was exploited for breast cancer detection over broadband spectral range (400~1650 nm) with two different classifier algorithms providing high sensitivity and specificity.²⁷

The breast tissue interacts with light according to its optical properties (type/size/density/color) to provide several mechanisms such as transmission, absorption, and diffuse reflectance.^{43,44} The main concern in this experiment was measuring the sample transmission to calculate the absorption to identify and characterize the breast samples regarding its spectral signature, as illustrated in Figure 1.

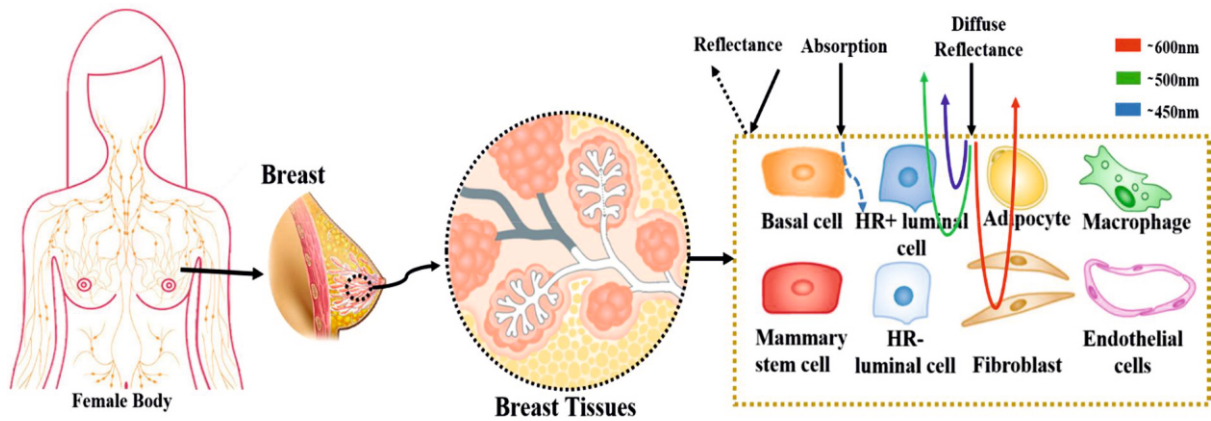


Figure 1. The light interaction (absorption / diffuse reflection / reflectance) of ex-vivo breast tissue sample highlighting the substitution of the breast tissue cells

In the proposed approach, we established a system that could provide promising outcomes regarding breast sample optical properties in both diagnostic and therapy applications. After exploring breast tissue optical properties (Transmission, absorption, and diffuse reflection), we could select the optimum wavelength for breast tissue therapy and diagnostic applications to assist the pathologist during the tissue investigation and reduce the time of examination and the surgeon during the breast biopsy and mastectomy process.

Methods

The main protocol used in this study is as follows:

- Sample investigation and tissue characterization.
- HS image for the *ex-vivo* breast sample.
- Measuring sample transmission transmission.
- Calculation of the sample absorption from the measured transmission.
- Measuring for sample diffuse reflection.
- Selection of the optimum wavelength for therapy.
- Selection of the spectral image to differentiate between the tumor and normal regions in the diagnostic applications. (Table 1)

Table 1. Patient’s charachterictics

| Patient ID | Age (years) | Breast structure ^a | Tumor size ^b | Grade ^c |
|------------|-------------|-------------------------------|---|--------------------|
| 1 | 52 | Extremely dense | Stage 1 (<2cm) | Grade I |
| 2 | 49 | Scattered dense | Stage 2 (<4cm) | Grade I |
| 3 | 55 | Heterogeneously dense | Stage 2 (<4cm) | Grade II |
| 4 | 44 | Mostly fatty | Stage 2 (<4cm) | Grade II |
| 5 | 46 | Scattered dense | Stage 3 (>4cm but confined to the breast) | Grade I |
| 6 | 50 | Heterogeneously dense | Stage 3 (>4cm but confined to the breast) | Grade II |
| 7 | 53 | Heterogeneously dense | Stage 1 (<2cm) | Grade I |
| 8 | 56 | Heterogeneously dense | Stage 3 (>4cm but confined to the breast) | Grade II |
| 9 | 58 | Heterogeneously dense | Stage 2 (<4cm) | Grade II |
| 10 | 60 | Extremely dense | Stage 2 (<4cm) | Grade I |

^a Breast Structure Type: Mostly fatty; Scattered density; Heterogeneously density; Extreme density

^b Tumor Stage: Stage 1 – A breast tumor is smaller than 2 centimeters in diameter and the cancer has not spread beyond the breast; Stage 2 – A breast tumor measures 2 to 4 centimeters in diameter or cancerous cells have spread to the lymph nodes in the underarm area; Stage 3 – More widespread cancer is found; however, it is confined to the breast, surrounding tissues.

^c Tumor Grade: Grade I - Well differentiated; Grade II - Moderately differentiated



The main framework of the proposed system is subdivided into two individual setups utilizing hyperspectral HS camera. Both setups exploited polychromatic source light with wavelength (380~1050 nm). The first setup (Transmission Mode) was applied for light transmission measurement of the *ex-vivo* breast sample. Thereby, calculations of sample absorption, as displayed in Figure 2-a. Second setup (Reflection

Mode) were exploited for the measurement of breast sample light diffuse reflectance, as illustrated in figure 2-b.

The results for the two setups were used to determine the optimum wavelength to differentiate between the normal and tumor regions in the *ex-vivo* breast samples using the optical properties spectroscopy in the Near and visible (NIR-VIS) spectrum.

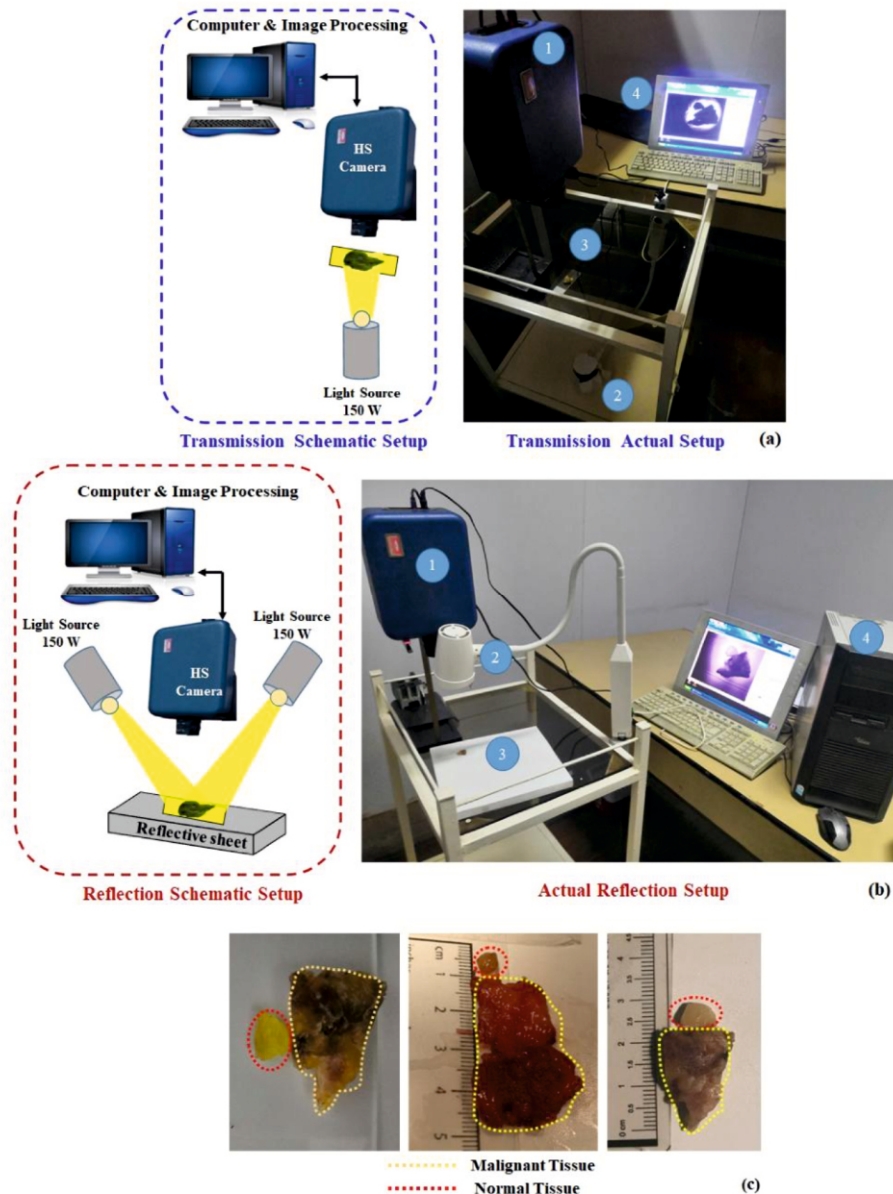


Figure 2. (a) System setup#1 (Transmission Mode - T) Measuring the optical properties (Transmission and absorption) of the *ex-vivo* breast sample, (1) The HS camera used (Surface Optics, SOC710, USA), (2) Polychromatic source light (Derungs, 150 W, 400~1000 nm, Germany), (3) The investigated *ex-vivo* breast sample, (4) Computer and image processing software (b) system setup#2 (Reflection Mode - R) Measuring the optical properties (Diffuse Reflection) of the *ex-vivo* Breast Sample, (c) Acquired RGB images for some of the *ex-vivo* breast samples in the experiments

Pathology examination and sample slicing for malignancy

Before the experimental investigation, the procedure validation was achieved from Ain Shams University - Ethics Committee. Overall, 10 patients who with breast cancer who had been underwent mastectomy were selected. Subsequently, after

careful examination and evaluation, the breast tumor samples were selected from arbitrary patients.

The investigated *ex-vivo* breast samples were crudely cut into slices with approximate sizes (2.5×3 cm), sample thickness 4~6 mm, then transported in icebox full of deionized saline. The samples were approximately (2.5×3 cm) slices at lab temperature

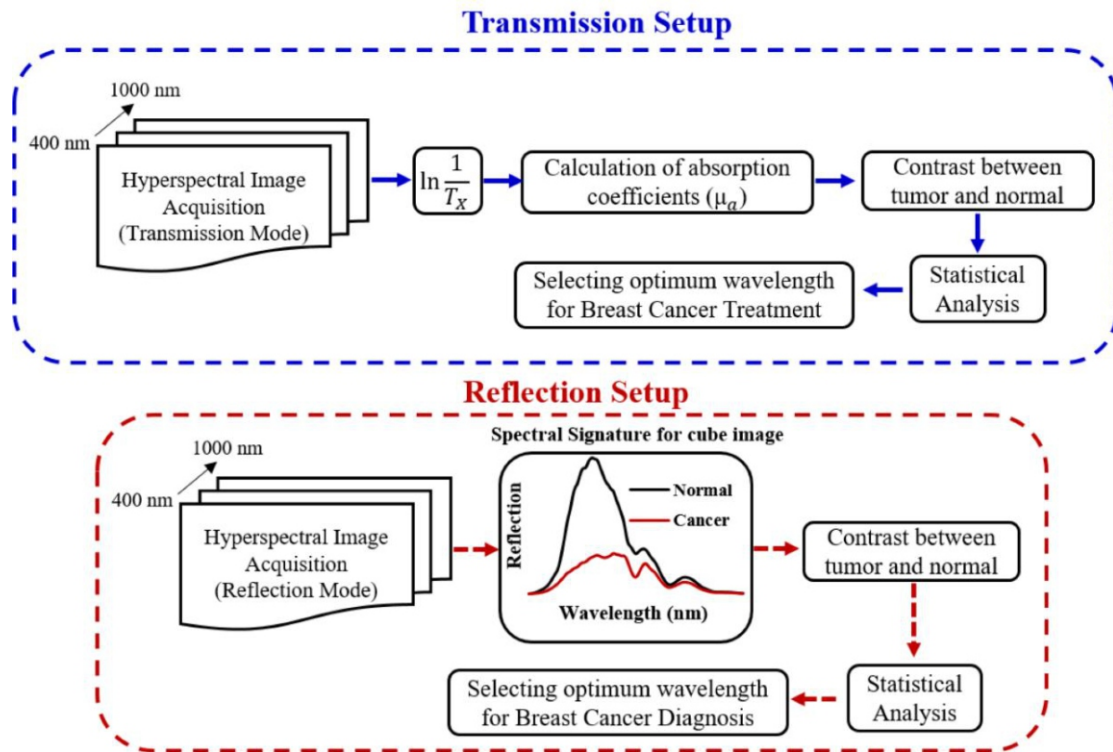


Figure 3. The image processing protocol for the two setups for ex-vivo breast tissue sample optical properties

23°C~ 24°C, and the temperature of the sample investigated was 25~28 °C. The samples were persevered before and after the trails at ~69 °C, as displayed in Figure 2-c.

The main theory and system equations

The main block diagram of the two system setups to measure the optical properties of the investigated breast samples is presented below. Transmission, absorption, and diffuse reflection were measured and then the custom algorithm was applied to increase the image contrast and delineate the tumor region of the samples, as depicted in Figure 4.

Light propagation in tissue is modeled based on transport theory^{45,46} which relies on the superposition of energy flux so that the wave properties of light (e.g. polarization, interference, etc.) are not considered. The radiant power of the light transferred in the surface is clarified in equation (1):

$$R = \int F \cdot n \quad (1)$$

Where, (F) is the flux vector, (R) is the radiant power transferred through a surface with the area (A).

Describing the propagation of light in turbid media, it is essential to explain some of the important optical parameters used in modeling light propagation in turbid media. Therefore, the propagation of photons, the radiance, fluence rate, and flux were considered.⁴⁷

The photon distribution function $N(r, \hat{s})$ is described as the number of photons per unit volume traveling in the route of a unit vector \hat{s} , in an element

of solid angle including \hat{s} , at a given point r divided by this element. The power of the photons (P) that propagate via the minute area dA in the minute solid angle $d\omega$ in the direction of \hat{s} , with energy $h\nu$ and velocity c_t is demonstrated in equation (2):

$$dP(r, \hat{s})[W] = N(r, \hat{s}) dA d\omega c_t h\nu \quad (2)$$

Where (c_t) is the velocity of light in tissue and (dA) is perpendicular to (\hat{s}).

Medical applications often involve the interaction of light with the tissue. The amount of light could be expressed as the irradiance E_0 , which is realized as the radiant energy flux incident on an element of the surface, divided by the area of the surface. Apart from that incident, light is reflected and tissue entrance is attenuated by scattering and absorption according to Beer's law, as highlighted in equation (3).

$$\phi(d) = E_0 (1-R) (e^{-(\mu_a + \mu_s)d}) \quad (3)$$

where $\phi(d)$ is the fluence rate for the un-scattered beam at position d , E_0 is the irradiance, and R is the Fresnel surface reflection.

$$\sigma = \frac{1}{(\mu_s + \mu_t)} = \frac{1}{\mu_t} \quad (4)$$

Where (μ^t) is the total attenuation coefficient and (σ) is the penetration depth.

The interface of the light beam with the biological tissues is assessed in terms of transmission measurement (T), diffuse reflection (R_d), and calculated attenuation absorption (A_t)⁴⁷, according to the following equations:



$$T = \frac{T_s - T_0}{T_{st} - T_0} \quad (5)$$

$$R_d = \frac{R_{d_s} - R_{d_0}}{R_{d_{st}} - R_{d_0}} \quad (6)$$

Where $\frac{R_{d_s}}{T_s}$ and $\frac{R_{d_{st}}}{T_{st}}$ are the light intensities measured by diffuse reflectance/transmittance with the breast sample and the standard reflecting optical white plate, respectively. The $\frac{R_{d_0}}{T_0}$ exemplifies the background light intensity distinguished by reflectance/transmittance without a sample on the reflecting plate.

Spectral planning and Procurement

To capture the necessary HSI data, we used HS camera (Surface Optics, SOC710, USA) with spectral resolution 3.1 nm equivalent to 600×502 pixels for the spectral group (HS Cube captured in 3.65 sec). The HSI was comprised of overall 128 spectral groups in range 379~1050 nm, incorporated with a lens with range (400~1000 nm). The camera was used with a lens (Schneider, 400~1000 nm, Germany). The light assembly for the HS image scan was used with polychromatic source light (150 W, 400~1000 nm).

Several scanned images for investigating the sample were acquired, and then statistical analysis

was done for the spectral signature to select the ideal spectral image, followed by the custom algorithm.

A basic advancement in HSI imaging, before image procurement, is a level field correction for data standardization. A white equalization and dim current measurements were utilized to gain relative reflectance from the sample.⁴⁸ The dark cube was captured by closing the HS camera lens with its cap to avoid any light getting into the sensor. Information from a dark image and white balance estimations were utilized to correct the deliberate material image. The fundamental reason for this amendment was to wipe out artifacts and noise impacts on the sample tissue, as clarified in equation (7):

$$RF(\vartheta) = \frac{Im(\vartheta) - Id(\vartheta)}{Iw(\vartheta) - Id(\vartheta)} \times 100\% \quad (7)$$

Where $RF(\vartheta)$ is the relative reflectance of the object image, $Im(\vartheta)$ is the captured image, $Id(\vartheta)$ is the dark acquired image with the lens shut with the cap, and $Iw(\vartheta)$ is the acquired image of the whiteboard.

We applied normalization on the captured image to remove the unwanted spectral impact from the polychromatic light. The original captured images vary depending on the light, the irregular shape of the sample, and temperature variations, so spectral images ought to be normalized including pixel normalization, as demonstrated in equation (8).

$$I_{new} = (I_{previous} - min_{previous}) \frac{max_{new} - min_{new}}{max_{previous} - max_{previous}} + min_{new} \quad (8)$$

Although, normalization alters an m-dimensional grayscale previous image

$I_{previous} : \{A\}$ with intensity assessments in the range minimum ($min_{previous}$) to maximum ($max_{previous}$) into a new image

$I_{new} : \{A\}$ with intensity values in the range minimum (min_{new}) to maximum (max_{new}).

Next, applying the moving average filter, the arithmetic means filter at kernel value 10 for noise reduction and image enhancement, we have:⁴⁹

$$f(X \times Y) = \frac{1}{qt} + \sum_{(r \times c) \in W} S(r \times c) \quad (9)$$

Where 'S' is the noisy image, $f(X \times Y)$ is the restored image, and "r" and "c" for the row and column coordinates respectively, within a window 'W' of size ' $q \times t$ ' where the process takes place.

A histogram is comparable in appearance to a bar graph and it is a graphical display of information that arranges a lot of information to visualize/count the quantity of events of information (frequency) over units of discrete intervals, named buckets or bins. Basically, the equation for histogram circumvents the territory of the bars and it is assessed using the summation of the result of the class interval's width and comparing frequency thickness of each class, as explained in equation (10):

$$\mathcal{H} = \sum_{i=1}^n \mathcal{C}w_i \times fD_i \quad (10)$$

Where the Area of Histogram is (\mathcal{H}), the class width is ($\mathcal{C}w$), and the frequency density is (fD).

Results

In this section, we illustrate the fundamental investigation outcomes. The primary objective of these examinations is to highlight the system capability to discriminate between the normal and malignant tumor regions of the investigated *ex-vivo* breast samples utilizing the biological tissues optical properties.

We established two different system setups utilizing hyperspectral (HS) camera and various excitation source light with wavelength (380~1050 nm) for this investigation. The first setup involved light transmission (T) measurement of *ex-vivo* breast sample to provide the necessary data for breast tumor therapy. The second setup involved the measurement of breast sample light diffuse reflectance (R_d), which provided the crucial information for breast tumor detection.

The outcomes of the two setups were used to select the optimum wavelength which could differentiate between the normal and cancer specific regions in the investigated breast sample by exploring the optical properties spectroscopy in the

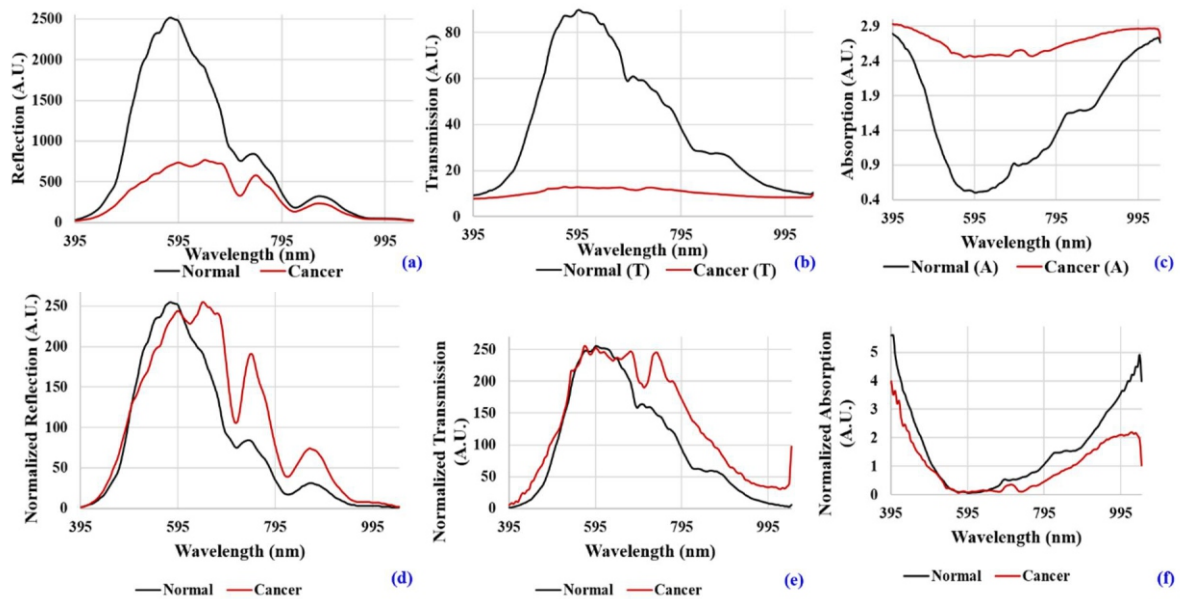


Figure 4. (a) The Diffuse reflectance (R) measurements of both the normal (black line) and cancer (red line) *ex-vivo* breast sample over the whole spectrum range; (b) The Transmission (T) measurements of both the normal (black line) and cancer (red line) *ex-vivo* breast samples over the whole spectrum range, (c) The Absorption (A) Calculations of both the normal (black line) and cancer (red line) *ex-vivo* breast samples over the whole spectrum range, (d) The Diffuse reflectance (R) measurements after applying normalization to the raw data to neglect the intensity effect and focus on the wavelength differentiation; (e) The Transmission (T) measurements after applying normalization to the raw data to neglect the intensity effect and focus on the wavelength differentiation; (f) The Absorption (A) Calculations after applying normalization to the raw data to neglect the intensity effect and focus on the wavelength differentiation.

Near and visible (NIR-VIS) spectrum.

The raw data displayed in figure 4-a, b, and c show the typical spectral values over the selected taken points on the malignant and normal regions. However, the raw data was normalized to neglect the variation of the intensity and focusing on the spectral change to display the spectroscopic point measurements, as

demonstrated in figure 4-c, d, and e.

Regarding the first setup (Transmission Mode) for light transmission (T) measurement of *ex-vivo* breast sample, we acquired 7-spectral images (400~1000 nm) with resolution 100 nm regarding the 128-frames to reduce the time consumption of image processing, as displayed in figure 5.

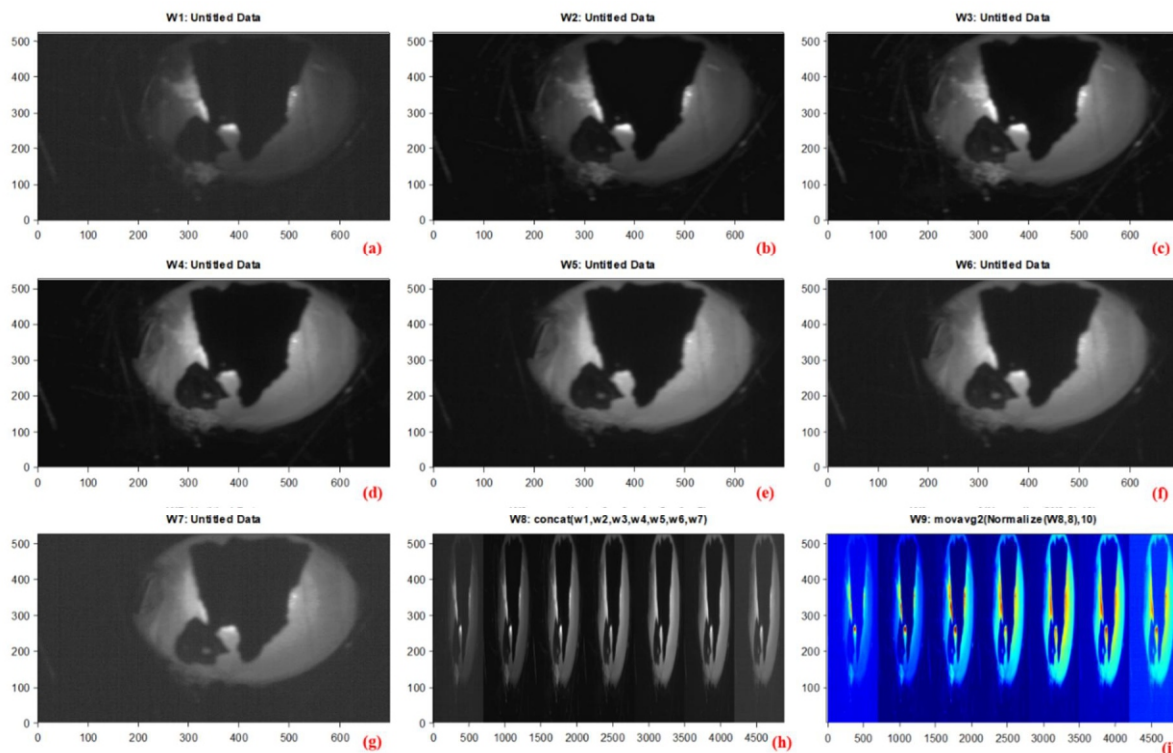


Figure 5. The Multiple Excitation Wavelength Light Source (380~1050 nm) generates Variable Transmitted Light through the *ex-vivo* Breast Sample, (a) Breast Sample at 400 nm, (b) Breast Sample at 500 nm, (c) Breast Sample at 600 nm, (d) Breast Sample at 700 nm, (e) Breast Sample at 800 nm, (f) Breast Sample at 900 nm, (g) Breast Sample at 1000 nm, (h) Conceded Image for the 7 wavelengths, (i) Conceded Image for the Image enhancement applying normalization and moving average filter ($K=10$) at scanned spectral images from (400 nm) to (1000 nm) with resolution 100 nm.

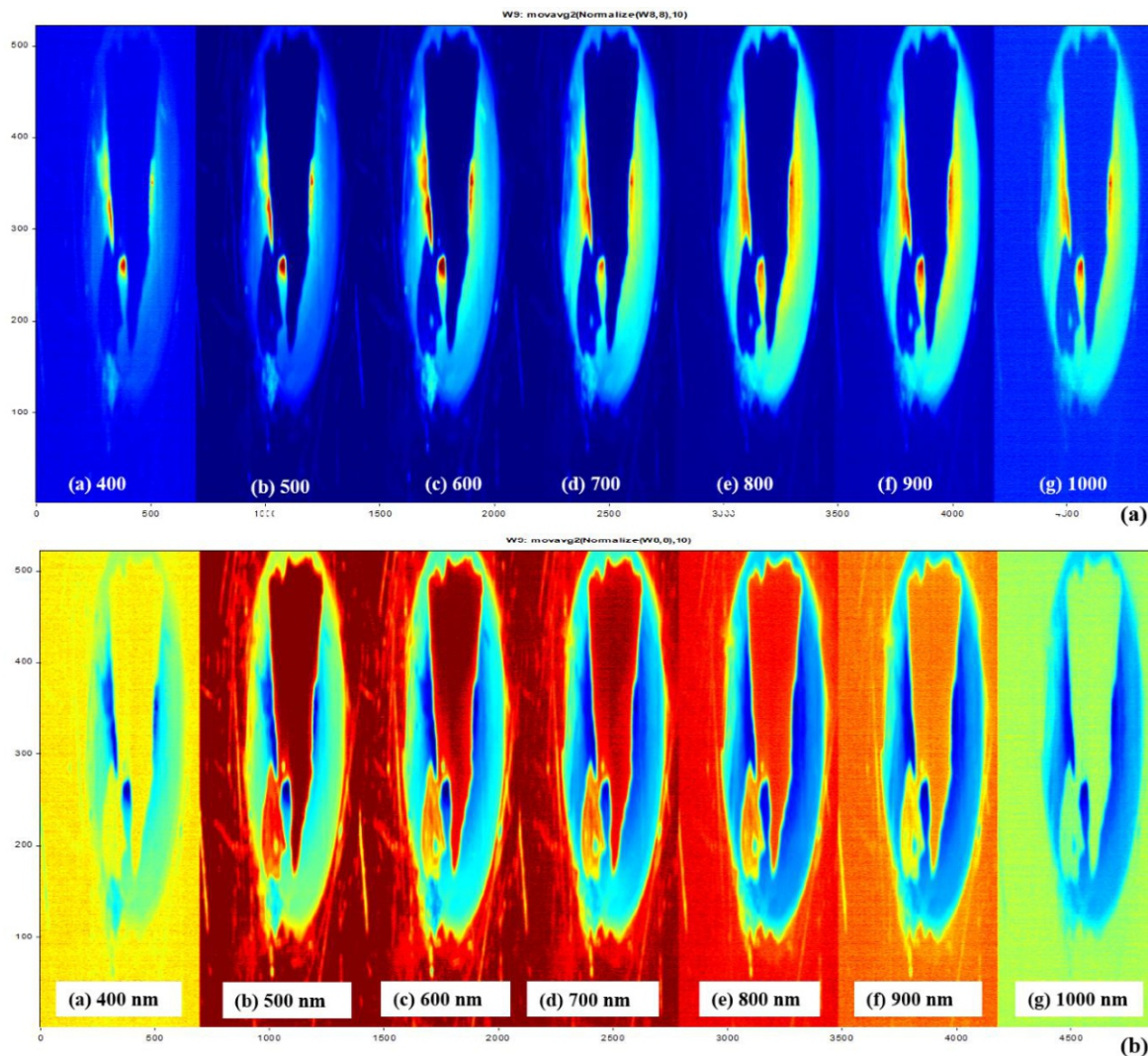


Figure 6. (a) The Conceded Image after Image enhancement for Variable Transmitted Light through the *ex-vivo* Breast Sample applying normalization and moving average filter ($K=10$) at scanned spectral images from (400 nm) to (1000 nm) with resolution 100 nm to differentiate between the malignant and normal tissue; (b) The Calculated Absorption Coefficient (A) from Variable Transmitted Light through the *ex-vivo* Breast Tissue under investigation at scanned spectral images from (400 nm) to (1000 nm) with resolution 100 nm to differentiate between the malignant and normal

The Conceded Image of the scanned spectral images (400~1000 nm) with resolution 100 nm were used after applying image enhancement, normalization and moving average filter ($K=10$) to differentiate between the malignant and normal tissue at variable Transmitted (T) Light through the *ex-vivo* Breast Sample as compared with the data from figure 45-b and figure 4-e as the spectral signature guidance to select the distinct spectral image, as presented in figure 6-a.

The Conceded Image of the attenuation absorption (A) to the spectral images (400~1000 nm) with resolution 100 nm was used after applying image enhancement, normalization, and moving average filter ($K=10$) to differentiate between the malignant and normal of *ex-vivo* Breast Sample as compared with the data from figure 4-c and figure 4-f as the spectral signature guidance to select the distinct spectral image, as exhibited in figure 6-b.

The second setup (Reflection Mode) was used for the measurement of breast sample light diffuse reflectance (R_d), as illustrated previously in figure 2-b. The experiment spectral signature demonstrated that the lowest measured diffuse reflection (R_d) at wavelength 400 nm and the highest at wavelength 560 nm could highly discriminate between the normal tissue and the malignant region, as can be seen in figure 7.

The Conceded Image of the sample light diffuse reflectance (R_d) at spectral images (400~1000 nm) with resolution 100 nm was used after applying image enhancement, normalization, and moving average filter ($K=10$) to remove the background noise to differentiate between the malignant and normal of *ex-vivo* Breast Sample as compared with the spectral signature in figure 4-a and figure 4-d, as displayed in figure 8.

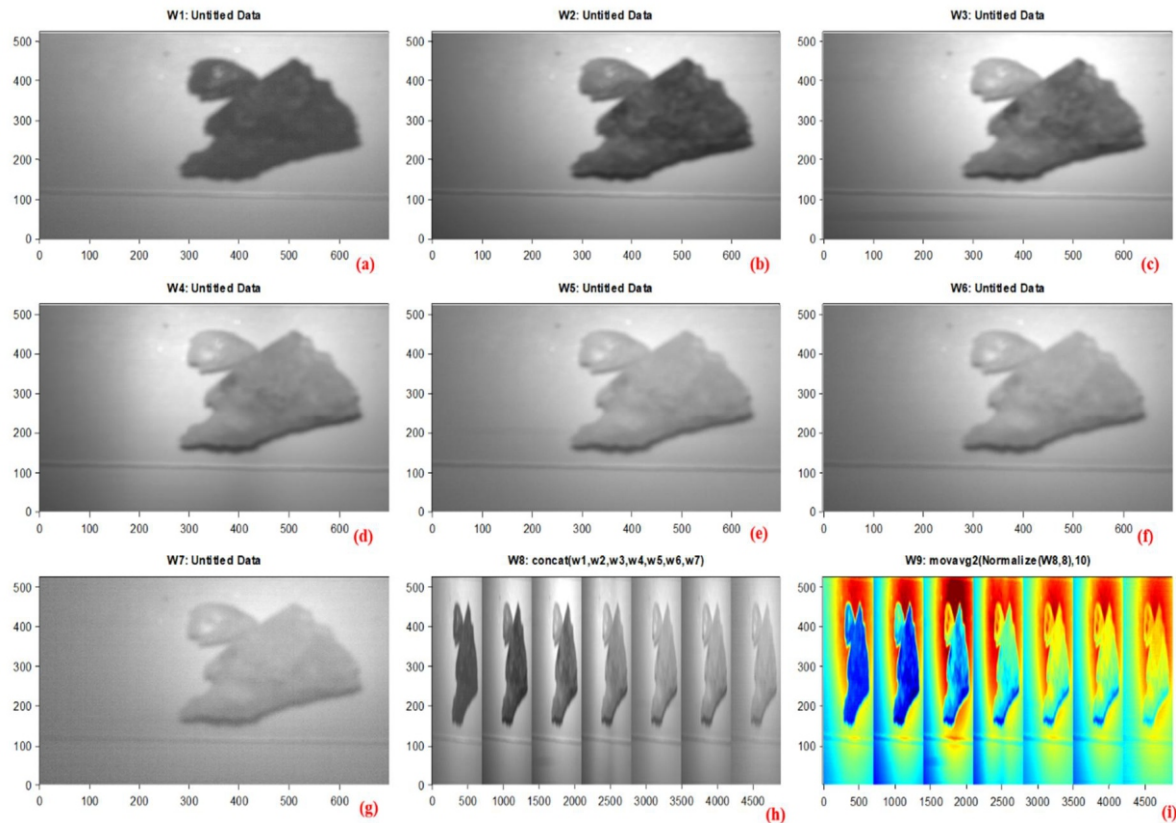


Figure 7. The measured diffuse reflectance (R_d) of the breast sample, (a) Breast Sample at 400 nm, (b) Breast Sample at 500 nm, (c) Breast Sample at 600 nm, (d) Breast Sample at 700 nm, (e) Breast Sample at 800 nm, (f) Breast Sample at 900 nm, (g) Breast Sample at 1000 nm, (h) Conceded Image for the 7 spectral images, (i) Conceded Image after the Image Enhancement applying normalization and moving average filter ($K=10$) at scanned spectral images from (400 nm) to (1000 nm) with resolution 100 nm.

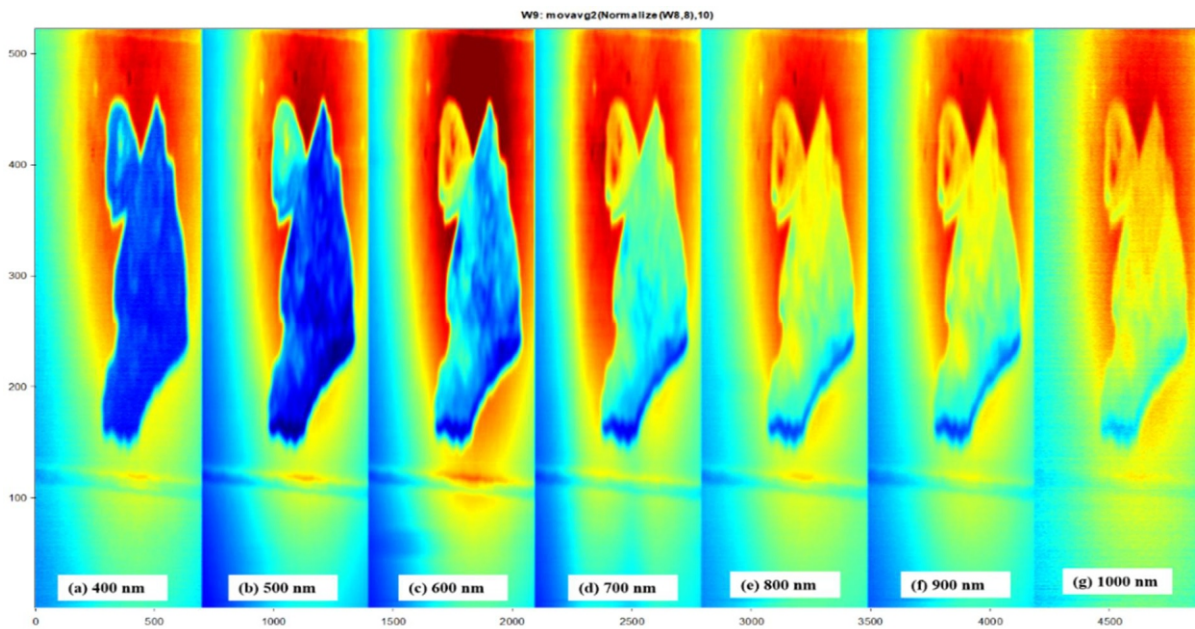


Figure 8. Conceded Image for the measured diffuse reflectance of the breast sample after Image Enhancement applying normalization and moving average filter ($K=10$) at scanned spectral images from (400 nm) to (1000 nm) with resolution 100 nm.

From figure 7 and 8, we could select the optimum spectral image by measured light diffuse reflectance (R_d), which had enough contrast to discriminate between the normal tissue and the malignant region which was at wavelength 600 nm. However, the results from the spectral signature in figure 4-a and

figure 4-d at wavelength 560 nm validated the outcome.

The HS image at wavelength (400 nm) represented the DC image which could not discriminate between the normal and the tumor regions, as shown in figure 9-a. The ideal HS image

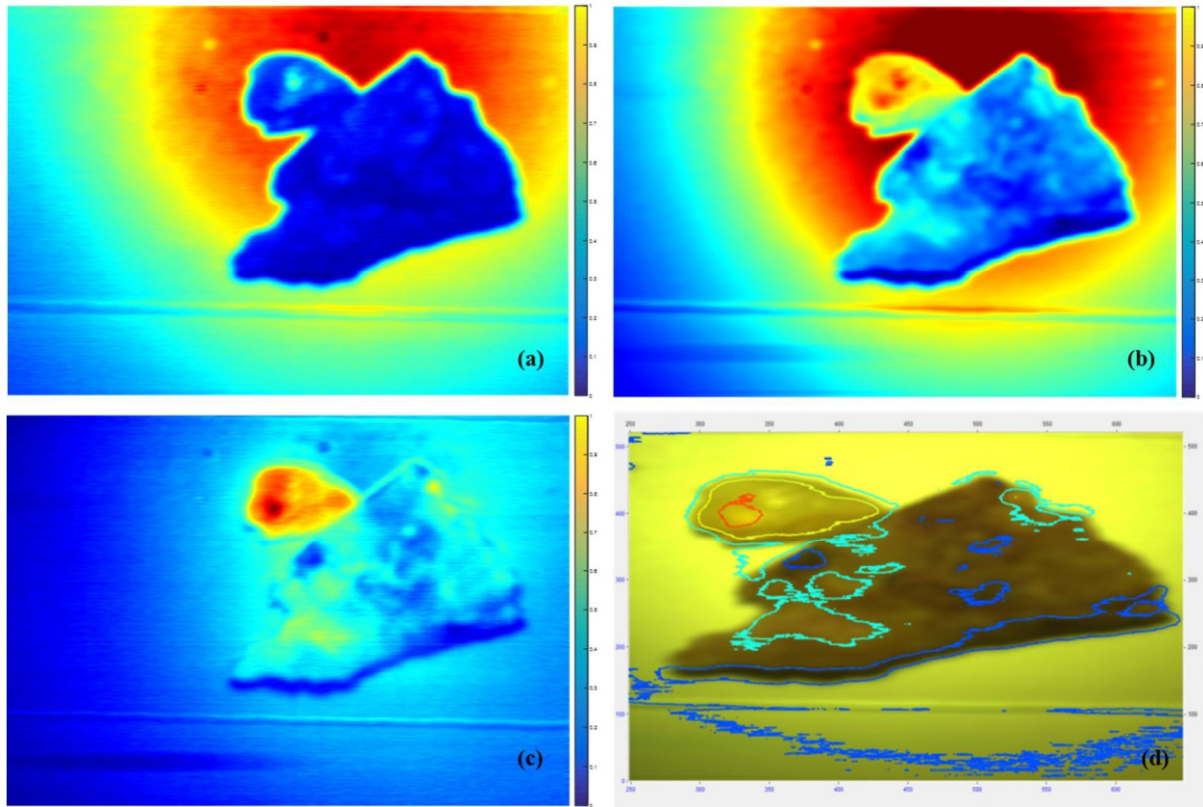


Figure 9. The *ex-vivo* breast Investigated Sample, (a) The HS Image of the breast sample at 400 nm , (b) The HS Image of the breast sample at 600 nm, (c) The subtracted Image between the (400 nm and 600 nm) to remove the DC background noise, (d) The Contour Mapping of the variable threshold regions of the tumors in the breast sample.

was at wavelength (600 nm) applied for ideal distinction between the normal and the tumor regions, as verified and calculated previously and displayed in figure 9-b. The subtracted image at figure 9-c is considered to be the ideal information for the specialized which could be used to identify the normal region (highly illuminated in the left) and the tumor regions (the more darker regions).

Finally, figure 9-d illustrates the contour mapping of the variable regions of the malignant breast which could be delineated according to the variable threshold value.

Discussion

Cancer is the second leading cause of death after heart disease as it continues to threaten the lives of millions worldwide.^{1, 2} Breast malignant growth is one of the most broadly perceived dangerous tumors in the world and the primary source of death among women.³ There is an expanding interest in improving breast cancer identification techniques using clinical imaging instruments because effective treatment of breast cancer relies upon its correct and early diagnosis.²⁴ Fundamentally, we can recognize early tumors before the tumor metastasizes.⁵⁰

We investigated the optical properties of the breast tissue utilizing the capability of the hyperspectral camera in the (NIR-VIS) spectrum. A set of spectrum images among (400~1000 nm) from recently excised breast tissues were investigated using two

approaches: (1) (Transmission Mode) was applied for light transmission (\mathbb{T}) measurement and (2) (Reflection Mode) used for measurement of breast sample light diffuse reflectance (R_d). The outcomes of both methods were used to select the optimum wavelength to differentiate between the normal and tumor regions in the *ex-vivo* breast sample by exploring the optical properties spectroscopy in the (NIR-VIS) spectrum, as demonstrated in figure 4.

The raw data displayed in the graph of figure 4-a,b, and c showed the typical spectral values over the selected taken points on the malignant and normal regions. However, the raw data was normalized to neglect the variation of the intensity and focusing on the spectral change to display the spectroscopic point measurements, as demonstrated in figure 4-c, d, and e

Figure 5 shows the first setup (Transmission Mode) for light transmission (\mathbb{T}) measurement of *ex-vivo* breast sample. We acquired 7-spectral images (400~1000 nm) with resolution 100 nm regarding the 128-frames to reduce the time of image processing. We noticed that the optimum spectral image was highly contrasted at wavelength 700 nm for light transmission (\mathbb{T}) measurement and verified in the attenuation absorption (A) as shown in figure 6-b. However, the results of the statistical analysis regarding the raw data signal in figure 4- c indicate the optimum wavelength at 600 nm, although the normalized data from Figure 4-f was more clearly identified in wavelength 760 nm, as illustrated in table 2.



Table 2. The Measurement of Breast tissue transmission (T) to highlight the highest contrast between the normal and cancer regions over the spectrum range.

| Wavelength (nm) | 400 | 440 | 480 | 520 | 560 | 600 | 640 | 680 | 720 | 760 | 800 | 840 | 880 | 920 |
|------------------------------------|-------|-------|-------|-------|-------|-------|-------|-------|-------|-------|-------|-------|-------|-------|
| Breast tissue transmission (T) | 9.3 | 12.6 | 25.0 | 51.6 | 82.6 | 89.6 | 83.5 | 66.7 | 59.0 | 49.9 | 36.4 | 28.0 | 26.6 | 18.7 |
| Cancer tissue transmission (T) | 8.0 | 8.4 | 9.4 | 10.5 | 12.2 | 12.6 | 12.3 | 12.5 | 12.0 | 11.8 | 11.0 | 10.1 | 9.6 | 8.9 |
| Standard Deviation ($\$d$) | 0.95 | 2.98 | 11.04 | 29.03 | 49.78 | 54.42 | 50.31 | 38.35 | 33.23 | 26.97 | 17.96 | 12.67 | 12.05 | 6.95 |
| ($\$d$) after Normalization | 4.495 | 12.73 | 22.63 | 3.54 | 2.83 | 3.54 | 0.71 | 42.43 | 42.43 | 69.31 | 55.15 | 41.01 | 25.46 | 18.38 |

Table 3. The measured diffuse reflectance (R_d) of the *ex-vivo* breast sample of the breast tissue to highlight the highest contrast between the normal and cancer tissue at the various spectrum range

| Wavelength (nm) | 400 | 440 | 480 | 520 | 560 | 600 | 640 | 680 | 720 | 760 | 800 | 840 | 880 | 920 |
|------------------------------------|-------|-------|--------|--------|---------|---------|--------|--------|--------|--------|--------|-------|-------|-------|
| Breast tissue reflection (R_d) | 40.2 | 174.2 | 695.3 | 1777.9 | 2334.9 | 2420.5 | 1933.9 | 1236.6 | 783.6 | 729.8 | 570.4 | 241.0 | 311.6 | 144.3 |
| Cancer tissue reflection (R_d) | 23.3 | 80.1 | 270.8 | 466.9 | 607.2 | 727.1 | 745.8 | 711.9 | 372.5 | 499.8 | 383.2 | 175.1 | 221.6 | 100.2 |
| Standard Deviation ($\$d$) | 11.95 | 66.50 | 300.13 | 927.03 | 1221.63 | 1197.36 | 840.08 | 370.95 | 290.70 | 162.63 | 132.34 | 46.63 | 63.67 | 31.18 |
| ($\$d$) after Normalization | 0 | 4.243 | 12.02 | 19.09 | 25.46 | 2.12 | 37.48 | 79.903 | 30.406 | 65.56 | 26.16 | 22.63 | 28.99 | 28.99 |

Figure 7 and Figure 8 displaying the acquired images regarding the second setup (Reflection Mode) to measure the Diffuse reflectance (R_d) measurements which emphasize the differentiation between the normal tissue and cancer region at wavelength 600 nm. Additionally, the statistical analysis of the raw data from figure 4-a show high contrast at wavelength 560 nm and after normalization it was more identified at 680 nm, as can be seen in table 3.

After selecting the optimum wavelength to differentiate between the normal and malignant tissue of the breast samples in the diagnostic applications by measuring the light diffuse reflection (R_d) at wavelength 600 nm, we removed the ground noise by spectral subtraction of spectral image at 400 nm to increase the contrast image, as shown in figure 9-c. Finally, figure 9-d illustrates the contour mapping of the variable regions of the breast malignant which could be used to delineate the cancerous regions in with variable threshold.

In conclusion, the results of this prospective approach revealed the HSI capability to be a feasible method to differentiate between the normal tissue and breast tumor, by providing vital information on the measurements of breast tissue optical properties in both the diagnostic and therapy applications. The experimental results by measurement of the diffuse reflectance (R_d) showed the optimum spectral image at 600 nm for the diagnostic applications. However, the statistical calculation of the normalized signal validated the outcome at wavelength 680 nm. Additionally, the optimum spectral image was obtained at 700 nm for the therapy applications by the measurement of breast tissue transmission (T) and absorption (A) calculation. Moreover, the statistical calculation of the normalized signal validated the outcome at wavelength 760 nm. In future work, we will update the system hardware such as the HS camera and increase the source light wavelength range. Additionally, we will use a Q-

switched pulsed laser at a custom optical system (760 nm) for breast tumor ablation without normal tissue damage.

Conflicts of interest

The authors declare no conflict or competing interests.

Ethics approval

All experimental and investigation trails were approved and validated by "Ain Shams University" Medical College Ethics Committee.

References

1. Murphy SL, Xu J, Kochanek KD. National vital statistics reports. National vital statistics reports. 2013;61(4).
2. Heron MP. Statistics, National Vital Statistics Reports Deaths: leading causes for 2017. 2019.
3. Bray F, Ferlay J, Soerjomataram I, Siegel RL, Torre LA, et al. Global cancer statistics 2018: GLOBOCAN estimates of incidence and mortality worldwide for 36 cancers in 185 countries. *CA Cancer J Clin.* 2018;68(6):394-424.
4. DeSantis CE, Miller KD, Dale W, Mohile SG, Cohen HJ, et al. Cancer statistics for adults aged 85 years and older, 2019. *CA Cancer J Clin.* 2019;69(6):452-67.
5. Cheng H-D, Shan J, Ju W, Guo Y, Zhang L. Automated breast cancer detection and classification using ultrasound images: A survey. *Pattern recognition.* 2010;43(1):299-317.
6. Saravanan D, Joseph D, Vaithyasubramanian S. Effective Utilization of Image Information Using Data Mining Technique. *Recent Trends and Advances in Artificial Intelligence and Internet of Things: Springer; 2020.* p. 207-15.
7. Brem RF, Lenihan MJ, Lieberman J, Torrente J. Screening breast ultrasound: past, present, and future. *American Journal of Roentgenology.* 2015;204(2):234-40.



8. Team TACSmaec. Breast Cancer Early Detection and Diagnosis 2019 [Available from: <https://www.cancer.org/cancer/breast-cancer/screening-tests-and-early-detection/american-cancer-society-recommendations-for-the-early-detection-of-breast-cancer.html>].
9. International Agency for Research on Cancer (IARC). Latest global cancer data: Cancer burden rises to 18.1 million new cases and 9.6 million cancer deaths in 2018. [Available from: www.who.int/cancer/PRGlobocanFinal.pdf].
10. Boyd NF, Martin LJ, Yaffe MJ, Minkin S. Mammographic density and breast cancer risk: current understanding and future prospects. *Breast Cancer Res.* 2011;13(6):223.
11. Gøtzsche PC, Jørgensen KJ. Screening for breast cancer with mammography. *Cochrane database of systematic reviews.* 2013(6).
12. Kelly KM, Dean J, Comulada WS, Lee S-J. Breast cancer detection using automated whole breast ultrasound and mammography in radiographically dense breasts. *European radiology.* 2010;20(3):734-42.
13. Hambly NM, Liberman L, Dershaw DD, Brennan S, Morris EA. Background parenchymal enhancement on baseline screening breast MRI: impact on biopsy rate and short-interval follow-up. *AJR Am J Roentgenol.* 2011;196(1):218-24.
14. Brennan S, Liberman L, Dershaw DD, Morris E. Breast MRI screening of women with a personal history of breast cancer. *AJR Am J Roentgenol.* 2010;195(2):510-6.
15. Mehnati P, Tirtash MJ. Comparative Efficacy of Four Imaging Instruments for Breast Cancer Screening. *Asian Pac J Cancer Prev.* 2015;16(15):6177-86.
16. Gutierrez RM, Cerquera E, Mañana G. MPGD for breast cancer prevention: a high resolution and low dose radiation medical imaging. *Journal of Instrumentation.* 2012;7(07):C07007.
17. Grosenick D, Rinneberg H, Cubeddu R, Taroni P. Review of optical breast imaging and spectroscopy. *J Biomed Opt.* 2016;21(9):091311.
18. Pisano ED, Gatsonis C, Hendrick E, Yaffe M, Baum JK, et al. Diagnostic performance of digital versus film mammography for breast-cancer screening. *N Engl J Med.* 2005;353(17):1773-83.
19. Hylton N. Magnetic resonance imaging of the breast: opportunities to improve breast cancer management. *J Clin Oncol.* 2005;23(8):1678-84.
20. Lord S, Lei W, Craft P, Cawson J, Morris I, et al. A systematic review of the effectiveness of magnetic resonance imaging (MRI) as an addition to mammography and ultrasound in screening young women at high risk of breast cancer. *European journal of cancer.* 2007;43(13):1905-17.
21. Your Guide to the Breast Cancer Pathology Report 2014 [Available from: https://www.breastcancer.org/cms_files/47/Breastcancerorg_Pathology_Report_Guide_2014.pdf].
22. Sahu A. Hyperspectral Imaging to Discern Malignant and Benign Canine Mammary Tumors: Temple University; 2012.
23. Ouyang Y, Tsui P-H, Wu S, Wu W, Zhou Z. Classification of Benign and Malignant Breast Tumors Using H-Scan Ultrasound Imaging. *Diagnostics.* 2019;9(4):182.
24. Alrahi S, Chan PM, Ho BC, Seah MD, Chen JJ, et al. Extent of margin involvement, lymphovascular invasion, and extensive intraductal component predict for residual disease after wide local excision for breast cancer. *Clinical Breast Cancer.* 2015;15(3):219-26.
25. Merrill AL, Coopey SB, Tang R, McEvoy MP, Specht MC, et al. Implications of New Lumpectomy Margin Guidelines for Breast-Conserving Surgery: Changes in Reexcision Rates and Predicted Rates of Residual Tumor. *Ann Surg Oncol.* 2016;23(3):729-34.
26. Vos EL, Jager A, Verhoef C, Voogd AC, Koppert LB. Overall survival in patients with a re-excision following breast conserving surgery compared to those without in a large population-based cohort. *European journal of cancer.* 2015;51(3):282-91.
27. Kho E, Dashtbozorg B, De Boer LL, Van de Vijver KK, Sterenberg HJ, et al. Broadband hyperspectral imaging for breast tumor detection using spectral and spatial information. *Biomedical optics express.* 2019;10(9):4496-515.
28. Esbona K, Li Z, Wilke LG. Intraoperative imprint cytology and frozen section pathology for margin assessment in breast conservation surgery: a systematic review. *Annals of surgical oncology.* 2012;19(10):3236-45.
29. Keating JJ, Fisher C, Batiste R, Singhal S. Advances in intraoperative margin assessment for breast cancer. *Current Surgery Reports.* 2016;4(4):15.
30. St John ER, Al-Khudairi R, Ashrafian H, Athanasiou T, Takats Z, et al. Diagnostic Accuracy of Intraoperative Techniques for Margin Assessment in Breast Cancer Surgery: A Meta-analysis. *Ann Surg.* 2017;265(2):300-10.
31. Adão T, Hruška J, Pádua L, Bessa J, Peres E, et al. Hyperspectral imaging: A review on UAV-based sensors, data processing and applications for agriculture and forestry. *Remote Sensing.* 2017;9(11):1110.
32. Bioucas-Dias JM, Plaza A, Camps-Valls G, Scheunders P, Nasrabadi N, et al. Hyperspectral remote sensing data analysis and future challenges. *IEEE Geoscience and remote sensing magazine.* 2013;1(2):6-36.
33. Robles-Kelly A, Huynh CP. Imaging spectroscopy for scene analysis: Springer Science



- & Business Media; 2012.
34. Xiong Z, Sun D-W, Zeng X-A, Xie A. Recent developments of hyperspectral imaging systems and their applications in detecting quality attributes of red meats: A review. *Journal of food engineering*. 2014;132:1-13.
 35. Moghaddam TM, Razavi SM, Taghizadeh M. Applications of hyperspectral imaging in grains and nuts quality and safety assessment: a review. *Journal of Food Measurement and Characterization*. 2013;7(3):129-40.
 36. Dale LM, Thewis A, Boudry C, Rotar I, Dardenne P, et al. Hyperspectral imaging applications in agriculture and agro-food product quality and safety control: A review. *Applied Spectroscopy Reviews*. 2013;48(2):142-59.
 37. Denstedt M, Bjorgan A, Milanič M, Randeberg LL. Wavelet based feature extraction and visualization in hyperspectral tissue characterization. *Biomedical optics express*. 2014;5(12): 4260-80.
 38. Lu G, Little JV, Wang X, Zhang H, Patel MR, et al. Detection of head and neck cancer in surgical specimens using quantitative hyperspectral imaging. *Clinical Cancer Research*. 2017;23(18): 5426-36.
 39. Han Z, Zhang A, Wang X, Sun Z, Wang MD, et al. In vivo use of hyperspectral imaging to develop a noncontact endoscopic diagnosis support system for malignant colorectal tumors. *Journal of biomedical optics*. 2016;21(1):016001.
 40. Neittaanmäki-Perttu N, Grönroos M, Tani T, Pölonen I, Ranki A, et al. Detecting field cancerization using a hyperspectral imaging system. *Lasers in surgery and medicine*. 2013;45(7):410-7.
 41. Aref MH, Aboughaleb IH, El-Sharkawy YH. Tissue characterization utilizing hyperspectral imaging for liver thermal ablation. *Photodiagnosis and Photodynamic Therapy*. 2020;31:101899.
 42. Aboughaleb IH, Aref MH, El-Sharkawy YH. Hyperspectral imaging for diagnosis and detection of ex-vivo breast cancer. *Photodiagnosis and Photodynamic Therapy*. 2020;31:101922.
 43. Tuchin V. Tissue optics and photonics: Light-tissue interaction II. *Journal of Biomedical Photonics and Engineering*. 2016;2(3):030201.
 44. Tuchin VV. Tissue optics and photonics: biological tissue structures. *Journal of Biomedical Photonics & Engineering*. 2015;1(1).
 45. DiPerna RJ, Lions P-L. Ordinary differential equations, transport theory and Sobolev spaces. *Inventiones mathematicae*. 1989;98(3):511-47.
 46. Rinzema K, Murrer L, Star W. Direct experimental verification of light transport theory in an optical phantom. *JOSA A*. 1998;15(8): 2078-88.
 47. Yavari N. *Optical spectroscopy for tissue diagnostics and treatment control*. 2006.
 48. Md Noor SS, Ren J, Marshall S, Michael K. Hyperspectral image enhancement and mixture deep-learning classification of corneal epithelium injuries. *Sensors*. 2017;17(11):2644.
 49. Kumar V, Gupta P. Importance of statistical measures in digital image processing. *International Journal of Emerging Technology and Advanced Engineering*. 2012;2(8):56-62.
 50. Saika K, Sobue T. Cancer statistics in the world. *Gan to kagaku ryoho Cancer & chemotherapy*. 2013;40(13):2475-80.